1. Title: Thermodynamically Tuned Nanophase Materials for Reversible Hydrogen Storage

Ping Liu (Primary Contact), John J. Vajo
HRL Laboratories, LLC
3011 Malibu Canyon Road
Malibu, CA 90265
Phone: (310) 317-5474; Fax: (310) 317-5840
E-mail: *pliu@hrl.com*; *vajo@hrl.com*

DOE Technology Development Manager: Ned Stetson
Phone: (202) 586-9995; Fax: (202) 586-9811
E-mail: Ned.Stetson@ee.doe.gov

DOE Project Officer: Paul Bakke
Phone: (303) 275-4916; Fax: (303) 275-4753
E-mail: Paul.Bakke@go.doe.gov

Contract Number: DE-FC36-05GO1506

Project Start Date: March 1, 2005

Project End Date: February 28, 2010

3. Executive Summary

This program was devoted to significantly extending the limits of hydrogen storage technology for practical transportation applications. To meet the hydrogen capacity goals set forth by the DOE, solid-state materials consisting of light elements were developed. Many light element compounds are known that have high capacities. However, most of these materials are thermodynamically too stable, and they release and store hydrogen much too slowly for practical use. In this project we developed new light element chemical systems that have high hydrogen capacities while also having suitable thermodynamic properties. In addition, we developed methods for increasing the rates of hydrogen exchange in these new materials.

The program has significantly advanced 1) the application of combined hydride systems for tuning thermodynamic properties and 2) the use of nanoengineering for improving hydrogen exchange. For example, we found that our strategy for thermodynamic tuning allows both entropy and enthalpy to be favorably adjusted. In addition, we demonstrated that using porous supports as scaffolds to confine hydride materials to nanoscale dimensions could improve rates of hydrogen exchange by > 50x. Although a hydrogen storage material meeting the requirements for commercial development was not achieved, this program has provided foundation and direction for future efforts. More broadly, nanoconfinment using scaffolds has application in other energy storage technologies including batteries and supercapacitors.

4. Objectives and accomplishments

The overall goal of this program was to develop a safe and cost-effective nanostructured light-element hydride material that overcomes the thermodynamic and kinetic barriers to hydrogen reaction and diffusion in current materials and thereby achieve > 6 weight percent hydrogen capacity at temperatures and equilibrium pressures consistent with DOE target values. Specific objectives and our actual accomplishments were:

Objective 1. Develop and implement hydride destabilization strategies for light-metal hydrides containing Li and Mg.
Accomplishments: approximately 20 new hydrogen storage systems were developed and tested including $LiBH_4/MgF_2$, $LiBH_4/MgCl_2$, $LiBH_4/MgI_2$, $LiBH_4/MgS$, $LiBH_4/MgSe$, $LiBH_4/Mg_2Si$, $LiBH_4/Mg_2Cu$, $LiBH_4/Mg_2NiH_4$, LiH/B_4C, $LiBH_4/Si$, $CaSiN_2$, $MgSiN_2$, LiBC, $Mg(BC)_2$, LiH/TiO_2, LiH/SiO_2, and $LiBH_4/SiO_2$.

Objective 2. Develop methods for efficient and controlled synthesis of thermodynamically tuned nanophase metal hydrides.
Accomplishments: synthesized nanoporous carbon materials (including carbon aerogels, direct cast mesoporous carbon, and reverse cast mesoporous carbon) as scaffolds for nanoscale hydride materials; developed methods for incorporating $LiBH_4$, MgH_2, and $LiBH_4/MgH_2$ into scaffolds.

Objective 3. Characterize the hydrogenation/dehydrogenation rates and hydrogen storage capacity in nanostructured destabilized hydride systems.
Accomplishments: tested the hydrogenation/dehydrogenation behavior of the systems listed above including full equilibrium measurements for the $LiBH_4/Mg_2NiH_4$ system; measured rates of dehydrogenation and cycling efficiency for nanostructured $LiBH_4$, MgH_2, and $LiBH_4/MgH_2$.

5. Project summary
5.1 Primary accomplishments
The primary accomplishments of this program are development of:

1. The $LiBH_4/Mg_2NiH_4$ destabilized hydride system
2. Nanoscale $LiBH_4$ by confinement in nanoporous scaffolds
3. Nanoconfinement of $LiBH_4/MgH_2$ destabilized hydride system

Each of these accomplishments is described below.

5.1.1 $LiBH_4/Mg_2NiH_4$ destabilized hydride system
Although light element hydrides have high hydrogen contents, thus far, no single compound has been identified that has the thermodynamic properties required to meet the DOE targets. To address this issue, we pursued a strategy in which combinations of stable hydrides with additional hydrides or compounds were used to form destabilized chemical systems. Many systems were studied including those listed above. The $LiBH_4/Mg_2NiH_4$ system was studied in detail because of its remarkable features that include: full reversibility, reaction through a direct low temperature kinetic pathway,

formation of a unique ternary boride phase, and low reaction enthalpy coupled with a low entropy.

Dehydrogenation of a mixture of $4LiBH_4 + 5Mg_2NiH_4$ is shown in Figure 1.

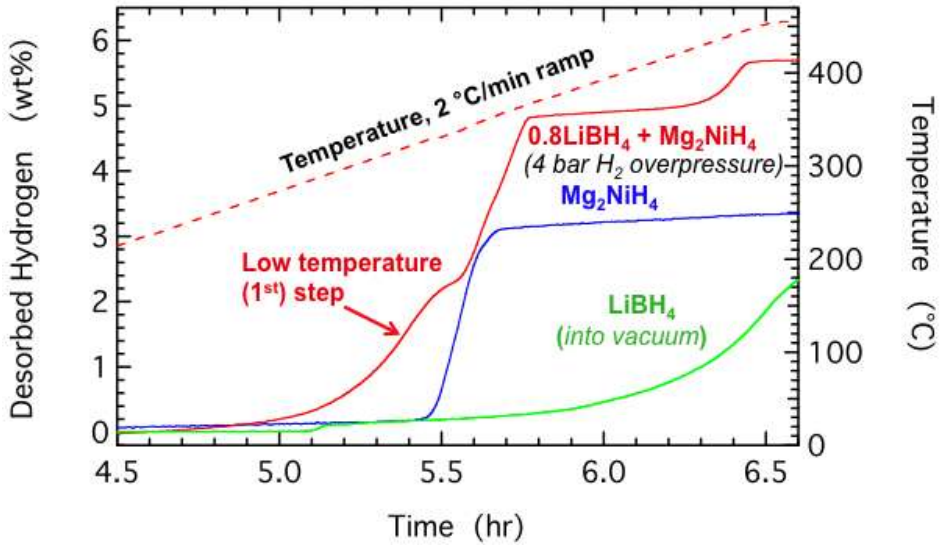

Figure 1. Dehydrogenation of $4LiBH_4 + 5Mg_2NiH_4$, Mg_2NiH_4, and $LiBH_4$. Dehydrogenation was conducted using a 2 °C/min temperature ramp in 4 bar of H_2 for $4LiBH_4 + 5Mg_2NiH_4$ and Mg_2NiH_4, and (initial) vacuum for $LiBH_4$. The small desorption step for $LiBH_4$ (at 5.1 hr) occurs at the melting point (~285 °C). Thus, the 1st step for the $4LiBH_4 + 5Mg_2NiH_4$ mixture begins below the melting point for $LiBH_4$.

The reaction occurs in 3 steps. The first step is consistent with the reaction given by

$$4LiBH_4 + 5Mg_2NiH_4 \leftrightarrow 2MgNi_{2.5}B_2 + 4LiH + 8MgH_2 + 8H_2$$

This reaction releases 2.6 wt% hydrogen. As shown in Figure 1, dehydrogenation occurs at temperatures lower than the dehydrogenation temperature for either pure $LiBH_4$ or pure Mg_2NiH_4. The behavior indicates that a new kinetic pathway is accessible in the mixture. This pathway likely involves direct reaction between $LiBH_4$ and Mg_2NiH_4. The reaction begins at temperatures as low as 250 °C, which is very low for borohydride-based systems. The low reaction temperature is possibly due to the catalytic nature of Ni in the $[NiH_4]^{2-}$ anion. Thus far, this system appears to be the only reversible destabilized system that reacts through a (new) direct reaction pathway. In contrast, the well-studied $LiBH_4/MgH_2$ system reacts sequentially with initial dehydrogenation of MgH_2 followed by reaction of Mg with $LiBH_4$. To achieve the full benefit of the mixed hydride system destabilization strategy, reaction through new kinetic pathways is essential. Thus, this system represents an important demonstration that such new pathways are possible.

As indicate above, reaction of $LiBH_4$ with Mg_2NiH_4 leads to the formation of the ternary boride $MgNi_{2.5}B_2$. This reaction sequence was carefully verified using x-ray diffraction, NMR, and FTIR measurements. In addition, we independently synthesized $MgNi_{2.5}B_2$ from MgB_2 + Ni and proved that the reaction could be initiated from either the hydrogenated ($4LiBH_4 + 5Mg_2NiH_4$) or partially dehydrogenated ($2MgNi_{2.5}B_2 + 4LiH + 8MgH_2$) phases. Formation of the ternary boride $MgNi_{2.5}B_2$ is significant because very few boride phases reversibly hydrogenate under mild conditions (<~ 100 bar H_2). In addition, ternary transition metal-based boride phases had not previously been considered as hydrogen storage materials. Identification of this phase suggests that other ternary (or

higher order) transition metal-based boride phases should be experimentally or computationally tested for reversible hydrogenation activity.

The equilibrium behavior for the $LiBH_4/Mg_2NiH_4$ reaction over the temperature range 270 °C to 360 °C is shown in Figure 2. This range extends below the lowest

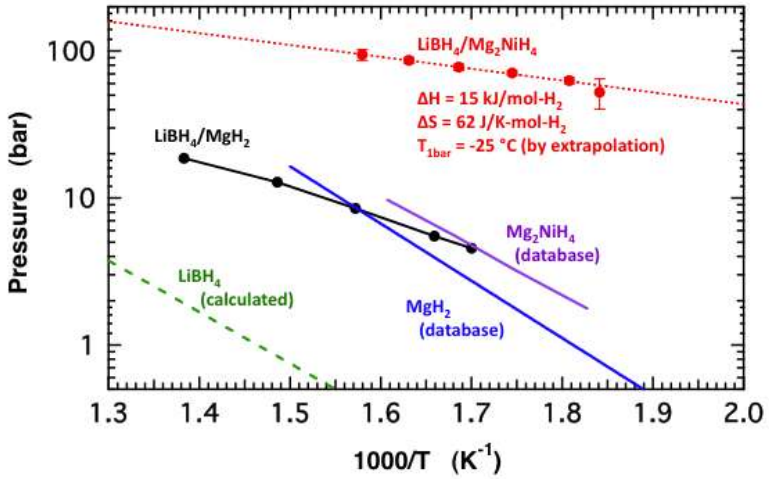

Figure 2. Van't Hoff plots for the $LiBH_4/Mg_2NiH_4$ destabilized system, pure $LiBH_4$, pure Mg_2NiH_4, the $LiBH_4/MgH_2$ system, and pure MgH_2. The red curve ($LiBH_4/Mg_2NiH_4$) shows equilibrium pressures at 0.67 wt% for the 1st reaction step shown in Fig. 1. This hydrogen content is at the midpoint of the reversible capacity for this step. The green curve ($LiBH_4$) was calculated from tabulated thermodynamic data using HSC. The blue and purple curves (MgH_2 and Mg_2NiH_4, recpectively) were obtained from the Sandia database. The black curve ($LiBH_4/MgH_2$) was obtained from measured isotherm data.

temperatures measured for the $LiBH_4/MgH_2$ system (315 °C) because of the improved kinetics, with the lowest temperature data point below the melting temperature for bulk $LiBH_4$ (T_m = 280 °C). The pressure varies logarithmically with the inverse temperature characterized by an enthalpy of 15 kJ/mol-H_2 and an entropy of 62 J/K-mol-H_2. This enthalpy is very low for a reversible system. A low enthalpy is very advantageous for practical systems in which heat must be supplied to release hydrogen and dissipated during rehydrogenation. However, systems with low enthalpies (<~ 30 kJ/mol-H_2) typically cannot be rehydrogenated because the equilibrium temperatures, given by $T_{eq} = \Delta H/\Delta S$, are too low. These low temperatures (<-100 °C) prevent hydrogenation because the rate of hydrogenation is too slow. Equivalently, at higher temperatures, where the rate of hydrogen exchange is faster, the equilibrium pressures are too high, >>100 bar H_2. Remarkably, for this system the entropy is also very low, which raises the equilibrium temperature and enables reversibility. We speculate that the low entropy originates from the relatively high entropy of two complex hydride anion species, $[BH_4]^-$ and $[NiH_4]^{2-}$, in the hydrogenated phase.

Overall, the capacity for the direct low temperature step shown above is too low for practical use. However, Mg_2NiH_4 is a transition metal-based complex hydride of which there are numerous (>100) known phases. Therefore, the remarkable behavior of this system holds promise that other $LiBH_4$/ transition metal-based complex hydride systems could be found with higher hydrogen capacities.

5.1.2. Nanoscale $LiBH_4$ by confinement in nanoporous scaffolds

One of the guiding hypotheses for this project was that the slow hydrogen exchange rates for light metal hydrides originate from slow rates of diffusion which, in turn, originate from the covalent and ionic bonding characteristic of light elements. Based on this hypothesis, we sought to improve the hydrogen exchange rates by restricting the hydride particle size to the nanometer scale. Diffusion times vary as the square of the diffusion length; thus, decreasing particle size by a factor of 10 decreases diffusion times by a factor of 100. Restricting the particle size of hydride materials is difficult considering that particle size growth occurs as hydrogen is cyclically released and stored. To address is issue, our approach was to use nanoporous scaffolds to confine hydride materials incorporated into the pores to nanoscale dimensions and to maintain these dimensions during cycling.

To characterize the effect of incorporating hydride materials into nanoporous scaffolds, dehydrogenation rates were measured for $LiBH_4$ incorporated into carbon aerogels with 4 nm and 25 nm pore sizes and compared with measurements on samples with 13 nm pores. The 4 nm sample was prepared at LLNL (Ted Baumann) while the 13 nm and 25 nm samples were prepared at HRL. Isothermal dehydrogenation measurements and pore size distributions are shown in Figure 3. Dehydrogenation of $LiBH_4$ was performed at 300 °C into a large volume, which kept the pressure below 0.1 bar. Maintaining the pressure low insured that the dehydrogenation was not inhibited by equilibrium. The 13 nm sample has the highest dehydrogenation rate, ~12.5 wt% $LiBH_4$/hr, while the 4 nm and 25 nm samples have lower rates, 7.8 wt% $LiBH_4$/hr and 6.8 wt% $LiBH_4$/hr, respectively. Comparing the 13 nm and 25 nm samples suggest that the kinetics are favored in smaller pores. This is the same trend that was seen using reaction temperatures determined by TGA. However, this trend does not extend to the 4 nm sample. In this case, the lack of micropores < 2 nm (see Figure 3b) in the 4 nm sample, may indicate the dehydrogenation nucleates in micropores. Alternatively, the lack of any relatively large pores may indicate the need for unfilled conduits for hydrogen transport. A third possibility is the influence of surface chemistry originating from slightly different synthesis routes at LLNL and HRL.

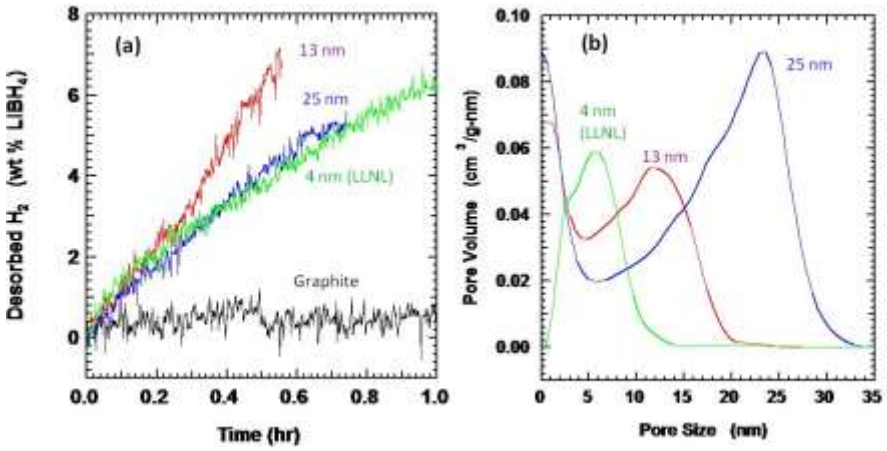

Figure 3. Effect of aerogel pore size and pore size distribution on the dehydrogenation rate of $LiBH_4$. Panel (a) shows the hydrogen desorbed in wt % $LiBH_4$ vs. time at 300 °C for $LiBH_4$ in 4 nm, 13 nm, and 25 nm aerogels and for $LiBH_4$ mixed with graphite. Panel (b) shows the pore size distributions for the aerogel samples.

Additional carbon scaffolds were also evaluated to maximize the kinetic impact while minimizing the volume and weight penalty. Shown in Figure 4a are SEM images of

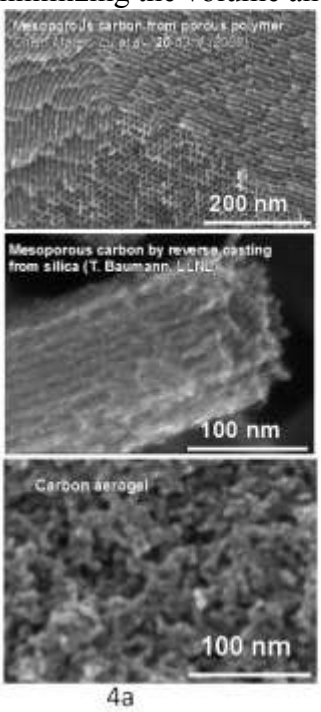

4a

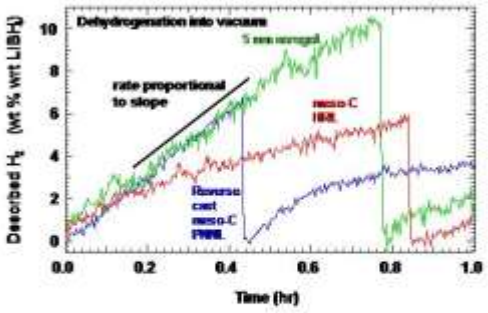

4b

Figure 4. (a) SEM images of mesoporous carbon synthesized from porous polymer (HRL meso-C) and reverse casting from mesoporous silica (by LLNL) and a carbon aerogel; (b) hydrogen desorption profiles for the carbon aerogel, HRL meso-C, and a mesoporous carbon from reverse casting prepared by PNNL which is similar to the LLNL material.

three representative carbon materials with distinct microstructures. Mesoporous carbon synthesized from porous polymer (HRL meso-C) has long, straight but not interconnected pores while the mesoporous carbon synthesized by reverse casting from mesoporous silica has long, straight but interconnected pores. The carbon aerogel, on the other hand, has isotropic random pores. These differences in architecture have a direct impact on hydrogen desorption kinetics as shown in Figure 4b. HRL meso-C has an initial rate very similar to those of aerogel and the reverse cast mesoporous carbon. However, unlike all the other materials, its rate gradually decreases with time. We could explain these observations by attributing them to the effect of the one dimensional porous architecture. As the dehydrogenation proceeds, the reaction products of LiH and B gradually accumulate in the pores, which impede the release of hydrogen. In contrast, carbon aerogels and the reverse cast mesoporous carbon both have three dimensional porous architectures which ensure continued hydrogen access. These results provide further evidence that porous architecture, in addition to pore size and pore volume, is an important factor in its effectiveness in kinetic enhancement.

The effect of nanoconfinement on the capacity retention during cycling was also studied; the results are shown in Figure 5. In bulk, the capacity retention of $LiBH_4$ is

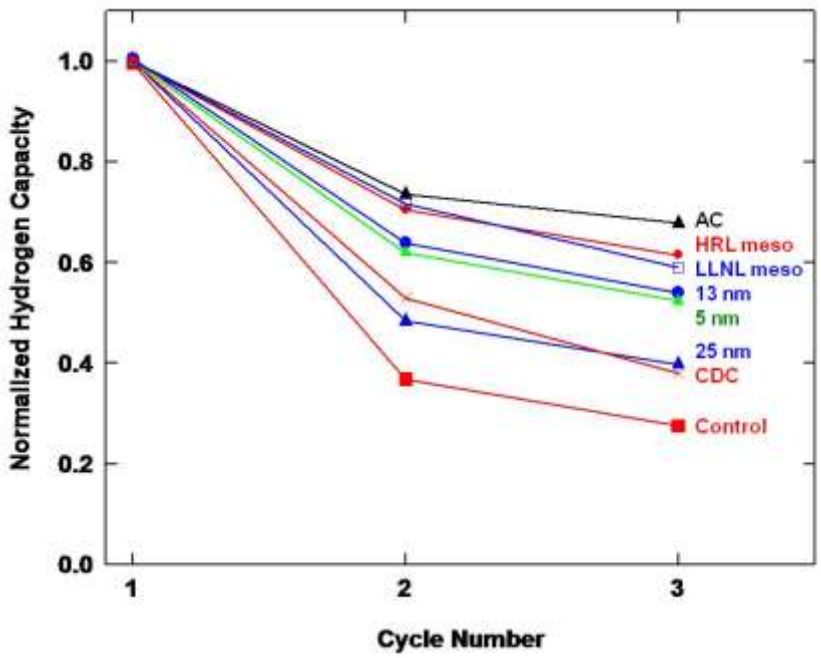

Figure 5. Cycling behavior of $LiBH_4$ confined within several nanoporous scaffolds. AC = activated carbon; HRL meso = direct cast mesoporous carbon; LLNL meso = reverse cast mesoporous carbon synthesized at LLNL; 5, 13, 25 nm = carbon aerogels with peaks in the pores size distributions at 5, 13, and 25 nm, respectively; CDC = carbide derived carbon obtained from Drexel University; control = physical mixture of $LiBH_4$ and 1 – 2 um graphite. Normalized capacities were determined by dehydrogenation during heating to 400 °C. Rehydrogenation was conducted at 100 bar H_2, 400 °C.

poor. After 3 cycles <30% of the capacity remains. In contrast, when confined within a nanoporous scaffold the retained capacity can be as high as 70%. The retention appears to improve with decreasing pore size with the best performance in activated carbon with < 2 nm pores, similar behavior for 5 nm and 13 nm pores, and degraded but still improved over bulk performance for 25 nm pores. Two samples with linear pores and very narrow pore size distributions performed nearly as well as the activated carbon.

In addition to altering the kinetics, the influence of nano-confinement on the equilibrium pressure was studied for $LiBH_4$ incorporated into a 13 nm mode pore size aerogel. As shown in Figure 6, at similar hydrogen contents, the hydrogen pressure at 300 °C for $LiBH_4$ confined within the aerogel reached ~3 bar while the pressure for $LiBH_4$ mixed with nonporous graphite rose to only ~0.3 bar. The results suggest a thermodynamic effect. Elucidation of the importance of the intermediate $Li_2B_{12}H_{12}$ offers a possible mechanism. The formation of $Li_2B_{12}H_{12}$ during dehydrogenation of bulk $LiBH_4$ has been unequivocally identified using NMR spectroscopy. This intermediate also occurs during dehydrogenation in the aerogel. In addition, DFT calculations indicate that formation of $Li_2B_{12}H_{12}$ according to the reaction

$12LiBH_4 \rightarrow Li_2B_{12}H_{12} + 10LiH + 13H_2$

occurs with an equilibrium pressure of ~11 bar at 300 °C. This pressure is of the same magnitude as the pressure measured for nano-confined $LiBH_4$. On the other hand, formation of elemental boron according to the reaction

$LiBH_4 \rightarrow LiH + B + 1.5H_2$

has an equilibrium pressure of 0.34 bar, which is close to the pressure measured for bulk $LiBH_4$. Thus, the effect of confinement may not be to alter the thermodynamics but rather to change the kinetic path by facilitating the path leading to $Li_2B_{12}H_{12}$.

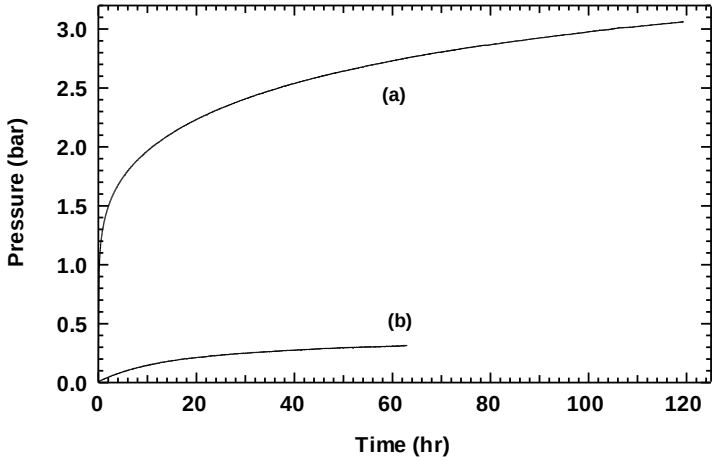

Figure 6: Long duration volumetric hydrogen desorption for $LiBH_4$ in porous and nonporous hosts at 300 °C. Curve (a) shows hydrogen desorption from $LiBH_4$ incorporated into a 13 nm aerogel. Curve (b) shows desorption from $LiBH_4$ mixed with nonporous graphite. The sample masses and desorption volumes were adjusted to prevent complete dehydrogenation. The final desorbed amounts were approximately equal: 4.5 wt% for Curve (a), and 3.9 wt% for Curve (b). These gravimetric capacities are calculated relative to the $LiBH_4$ weight only. The hydrogen pressure is ~10 times higher for $LiBH_4$ contained in the aerogel.

5.1.3. Nanoconfinement of $LiBH_4/MgH_2$ destabilized hydride system

To unify the thermodymanic tuning and nanoengineering aspects of the program (described individually above) we demonstrated the $LiBH_4/MgH_2$ destabilized system confined within a nanoporous carbon aerogel. The results are shown in Figure 7.

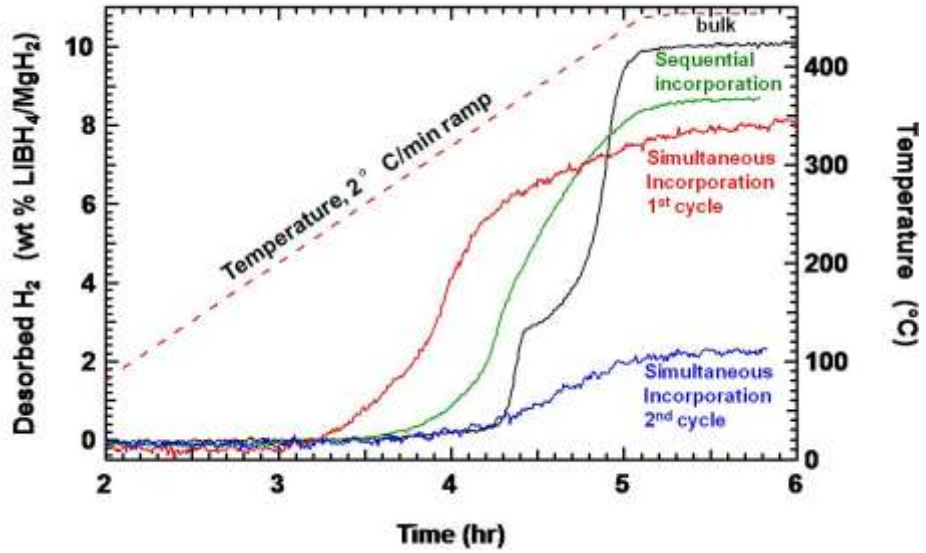

Figure 7. Dehydrogenation of $LiBH_4/MgH_2$ destabilized system during temperature ramp in 4 bar H_2. First cycle data are shown for bulk mixture (mechanically milled), system sequentially incorporated (with MgH_2 first) into a 13 nm aerogel, and system simultaneously incorporated into a 13 nm aerogel. Second cycle data also shown for simultaneously incorporated sample. Rehydrogenation between 1st and 2nd cycles conducted in 100 bar H_2 at 300 °C (2 hr) and 350 °C (4 hr).

In the bulk, the $LiBH_4/MgH_2$ system reacts in two steps: dehydrogenation of MgH_2 (which occurs at ~4.4 hrs in Figure 7) followed by reaction of Mg with $LiBH_4$ (~4.9 hrs). Upon sequential incorporation into a 13 nm pore size carbon aerogel with MgH_2 incorporated first, these two steps occur at lower temperatures and are more difficult to distinguish. Upon incorporation simultaneously, in which $LiBH_4$ and dibutyl Mg (a precursor to MgH_2) are rapidly precipitated by freezing from a common solvent, the reaction temperature is further lowered and only a single step is resolved. However, although the onset reaction temperature is reduced by ~100 °C, the cycling behavior when incorporated into the carbon scaffold is poor. This is shown by the low capacity for the 2nd cycle (Figure 7). The origin of the poor cycling is not understood. Further characterization is needed to determine if, in addition to improving the reaction kinetics, confinement within the aerogel also changes the reaction path.

To investigate whether any changes in reaction path were occurring, we characterized a sample of the full $LiBH_4/MgH_2$ destabilized system incorporated sequentially in a 13 nm carbon aerogel with ^{11}B NMR. Figure 8 shows the evolution of NMR spectra during two cycles of the hydrogen exchange reaction. After the 1st dehydrogenation, we observed the disappearance of the $LiBH_4$ signal and the appearance of three broad peaks. Two of the peaks can be attributed to MgB_2 and $[B_{12}H_{12}]^{2-}$ species, respectively. However, the third peak at ~ 30 ppm does not correlate with any compound known to us. This unknown phase appears to undergo reversible hydrogen exchange cycles. The reference spectrum of amorphous B (a-B) in the figure shows that the unknown phase is not a-B.

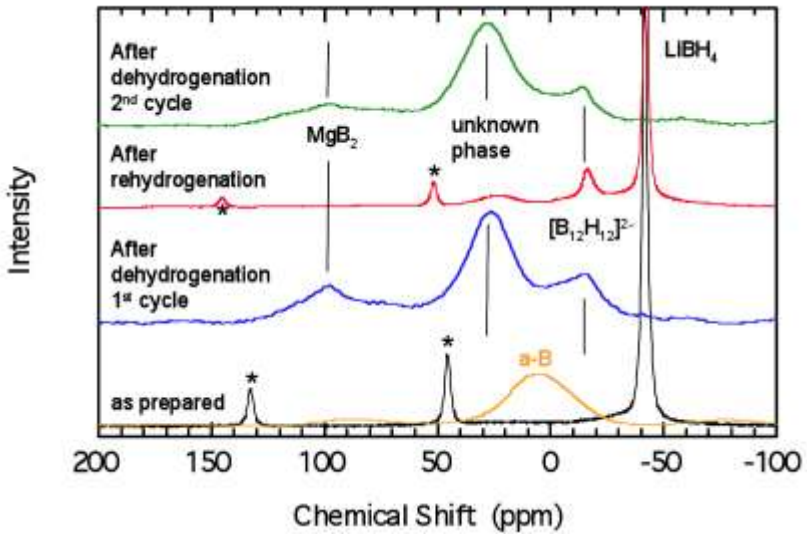

Figure 8: Evolution of NMR spectra for $LiBH_4/MgH_2$ in carbon aerogel during two cycles of hydrogen exchange reaction. The spectrum of amorphous B (a-B) is included for reference. In addition to the formation of MgB_2 and $[B_{12}H_{12}]^{2-}$ species, an unknown phase was observed at ~ 30 ppm. Asterisks' indicate spinning side bands.

To attempt to identify the 30 ppm ^{11}B NMR resonance, we measured several additional samples. $LiBH_4$ incorporated alone into an aerogel and dehydrogenated at 400°C and 450°C (Figure 9) showed the 30 ppm peak. After thermal treatment at 670°C in the presence of Mg, this peak further grew while the $B_{12}H_{12}$ species largely disappeared. The

same phenomenon takes place without the presence of Mg. We had hypothesized that this peak is likely associated with a boride with high B content due to the chemical shift value. We further attempted to identify the 30 ppm peak by comparing it to the spectra of $LiB_{0.9}$ and LiBC. The two compounds were synthesized and their phases were confirmed by XRD, which matched patterns in the ICDD database. However, as shown in Figure 9, these phases do not display an ^{11}B NMR resonance at 30 ppm. Since the chemical shift of the unknown peak is in between those of $LiB_{0.9}$ and LiBC, the compound could be $LiBC_x$, where $0<x<1$. Further work is needed to establish its exact composition.

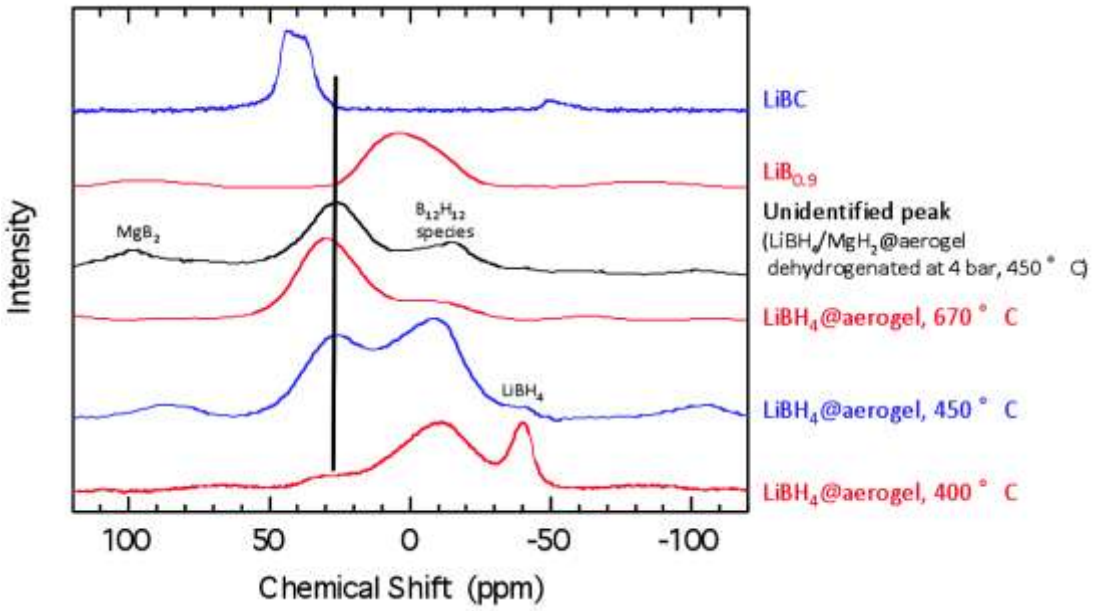

Figure 9: ^{11}B NMR spectra of $LiBH_4/MgH_2$ dehydrogenated in aerogel at 450 °C compared to $LiB_{0.9}$, LiBC, and $LiBH_4$ dehydrogenated in aerogel at 400 °C, 450 °C, and 670 °C.

5.2 Additional accomplishments

Additional accomplishments of this program include:

1. Study of the MgH_2/Si destabilized hydride system
2. The $LiBH_4$/MgX destabilized hydride systems
3. Study of destabilized systems containing C, Si, amides, or oxides
4. Study of nanoconfined MgH_2
5. Practical consideration of using scaffolds for nanoconfinement

Each of these accomplishments is described below

5.2.1 The MgH_2/Si destabilized hydride system

Considerable effort was devoted to exploring methods for enhancing kinetics in the MgH_2/Si system. Thermodynamic calculations (HSC) predict a dramatic decrease (>250°C) in T(1bar) when MgH_2 is destabilized by the addition of Si. This result, coupled with the fact that the MgH_2/Si system is readily amenable to nano-engineering by a variety of approaches, makes this a particularly interesting prototype system for study. The chemical reaction that describes destabilization of MgH_2 by the addition of Si is given as:

$2MgH_2 + Si \leftrightarrow Mg_2Si + 2H_2$.
In this case Mg_2Si forms as a stable alloy upon dehydrogenation, and the Mg_2Si phase must be converted back to the constituent components when the system is rehydrogenated. We have found that the kinetics in the forward direction (dehydrogenation) can be significantly enhanced by nano-engineering. For example, Figure 10 shows how the temperature for the onset of dehydrogenation can be decreased by the addition of nanoscale Ni as a catalyst and by the use of widely dispersed, small particles generated by energetic ball-milling of MgH_2 in an excess of Si ("dilution milling"). Compared with a reference (stoichiometric) sample that was formed by milling without Ni, we find that the onset temperature decreases by more than 100°C when the sample is prepared by dilution milling in the presence of 5% nano-Ni. Although dehydrogenation was improved, no rehydrogenation was observed.

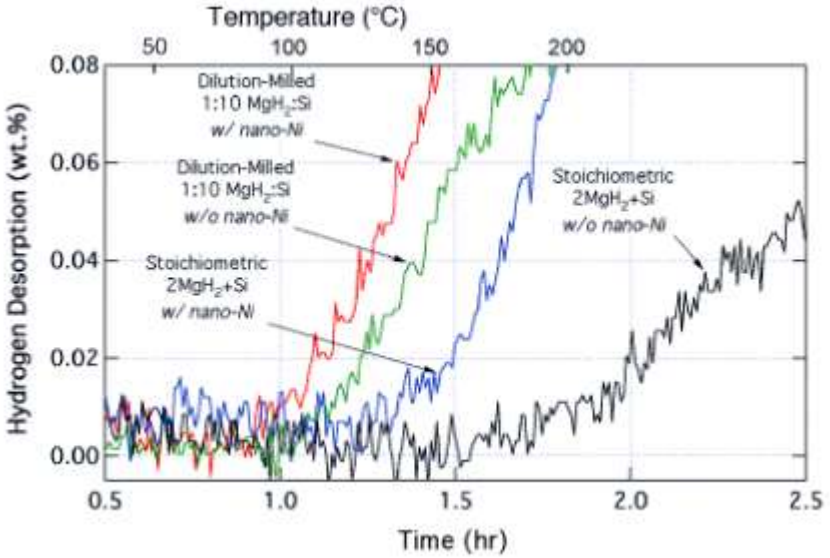

Figure 10: Effect of dilution milling and addition of Ni catalyst on the onset of hydrogen desorption in MgH_2/Si destabilized system. Ball-milled stoichiometric sample ($2MgH_2$+Si) with no added nano-Ni serves as reference. Desorption occurs at lower temperatures in stoichiometric sample containing 5% nano-Ni and in "dilution-milled" samples with and without Ni.

The effects of other catalysts and diluents on the dehydrogenation kinetics as well as on the hydrogenation of Mg_2Si were also studied. In addition to nanoscale-Ni, we evaluated the effects of nano-Mn and a nanoscale Ni-Co alloy on the dehydrogenation rate. Nanoscale Mn was selected because combinatorial analysis conducted at Intematix (an MHCoE partner) indicated that it might show improved catalytic performance. The Ni-Co alloy catalyst was chosen because investigators at QuantumSphere, Inc., a nanoparticle synthesis company (Santa Ana, CA), showed that Ni-Co is a high performance catalyst for PEM fuel cell applications. In both cases the catalyst particle size was $\leq$ 50 nm, and the catalyst concentration was maintained at 5% with respect to Mg. The MgH_2/Si samples were prepared in stoichiometric proportions, then milled for 5 hours at 400 rpm. After completion of the MgH_2/Si milling, the catalyst was added and the mixture was re-milled for 5 mins at 400 rpm. (The catalyst was milled for a much shorter time to ensure complete mixing without unwanted agglomeration or growth of catalyst particles). The amount of hydrogen desorption as a function of time for the Ni, Mn, and Ni-Co catalysts is given by the solid lines in Figure 11 (temperature vs. time is

given by the dashed line – r.h. ordinate). The onset and amount of desorption was comparable in all three samples, with nano-Ni exhibiting a slight performance advantage. We also explored the effect of different types of catalysts and diluents on hydrogenation of Mg_2Si. Three characteristically different additives were used: 1) Pd metal (10% w.r.t. Mg), a well-studied metal catalyst for hydride reactions; 2) V_2O_4 (5% w.r.t. Mg), a prototype metal-oxide catalyst; and 3) MgO (10x Mg in Mg_2Si), serving both as a diluent to create dispersed Mg_2Si particles within a larger quantity of MgO, as well as a metal oxide catalyst.

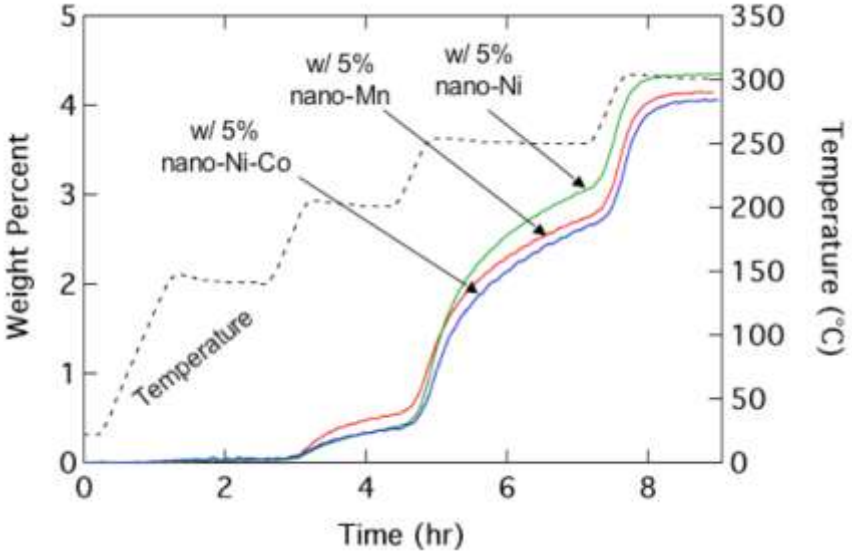

Figure 11: Hydrogen desorption from ball-milled MgH_2/Si containing three different nanoscale metal catalysts. Rate enhancement is comparable for all catalysts.

The three samples were prepared by milling a mixture of Mg_2Si powder (Aldrich) with the three different additives for 1 hour at 400 rpm. A dehydrogenation cycle was subsequently performed to ensure removal of residual hydrogen from the sample. Following hydrogenation at 200 bar H_2 at 150°C for 50 hrs, the samples were subjected to a second dehydrogenation cycle in the Sieverts apparatus, and the hydrogen desorption results are shown in Figure 12. In all cases, only a very small quantity hydrogen was released from the samples. The amount of desorbed hydrogen is calculated in Figure 12 with respect to the Mg_2Si weight only. Therefore it is possible that the release of hydrogen could be solely due to the additive and not due to MgH_2 formed by hydrogenation of Mg_2Si.

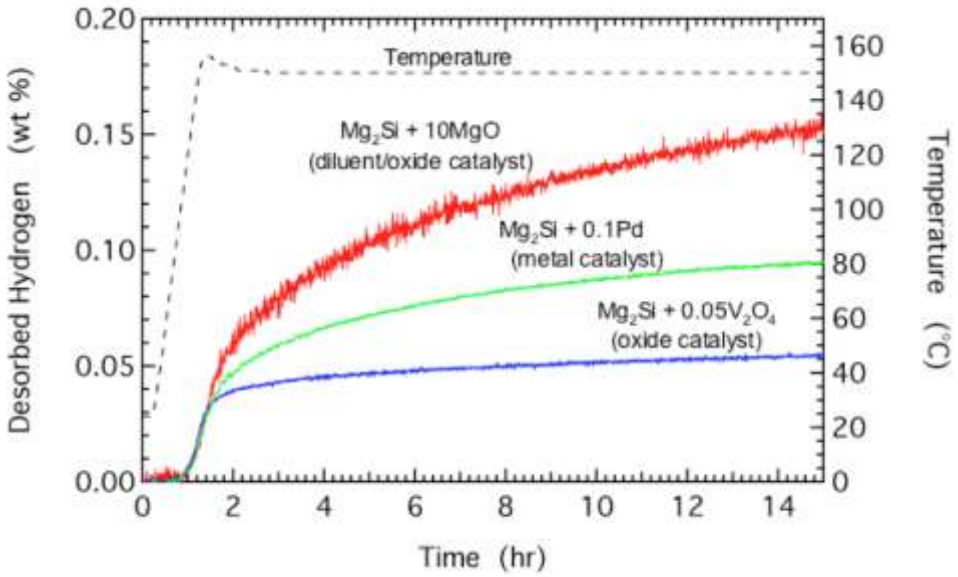

Figure 12: Effect of three different additives on the amount of desorbed hydrogen following hydrogenation of Mg_2Si at 200 bar, for 50 hrs at 150°C. The temperature-time profile for the dehydrogenation reaction is given by the dashed line (r.h. ordinate). The amount of desorbed hydrogen is calculated with respect to the weight of Mg_2Si. Minimal hydrogen desorption is observed for all samples.

Go-/No-Go Decision on MgH_2/Si Destabilized Hydride System

We were unable to obtain significant hydrogenation of Mg_2Si in any of the experiments that we conducted on during the course of this project. We investigated samples containing different catalysts, nano-scale samples formed from nano-particle precursors, and samples formed by a variety of other methods including: dilution-milling, self-propagating synthesis, powder metallurgy, and milling in hydrogen overpressure. We established conditions that facilitated dramatically improved rates of dehydrogenation from the MgH_2/Si system. However, all attempts to hydrogenate the Mg_2Si formed upon dehydrogenation have been unsuccessful.

Although thermodynamics calculations suggest that this system would be an good candidate for reversible storage applications (predicted T(1 bar) ≈ 40°C), kinetic barriers apparently preclude the hydrogenation reaction from occurring at accessible temperatures and pressures. Based upon the results from this work, it seems likely that phase separation (i.e. segregation and re-formation of MgH_2 + Si from reaction of Mg_2Si with hydrogen) is strongly inhibited in this reaction system. We believe that this is the primary reason for the lack of observable hydrogenation. Based upon these results, we terminated additional experimental work on the MgH_2/Si destabilized system – i.e., a "No-Go" decision on this system effective at the end of Quarter 4, FY06.

5.2.2 The $LiBH_4$/MgX destabilized hydride systems

To investigate new destabilized systems, we performed equilibrium calculations using a thermodynamics calculation program (HSC), for several candidate $LiBH_4$ + MgX (X= F, Cl, OH, O, S, Se, Si, Ge, and Ni) destabilized systems. We found gravimetric capacities ranging from 5 to 10 wt% with T(1 bar) = 0 to 400 °C. Partial reversibility was demonstrated in three systems:

- $2LiBH_4 + MgF_2 \leftrightarrow 2LiF + MgB_2 + 4H_2$ (7.6 wt.%, $T_{1\ bar}$=150°C)

(H_2 uptake ~6.5% at 325°C; dehydrogenation 5.3%)

- $2LiBH_4 + MgS \leftrightarrow Li_2S + MgB_2 + 4H_2$ (8.0 wt.%, $T_{1\ bar}$ =170°C))

(H_2 uptake ~6% at 350°C; dehydrogenation ~4.3%; 2nd cycle uptake <4%)

- $2LiBH_4 + MgSe \leftrightarrow Li_2Se + MgB_2 + 4H_2$ (5.4 wt.%, $T_{1\ bar}$ =70°C)

(H_2 uptake ~4.5% at 350°C; dehydrogenation ~3.3%)

Although the thermodynamics calculations were encouraging, we found that experimentally measured sorption temperatures were much higher than HSC predictions of T(1bar) in virtually all of these systems (see Table 1). This discrepancy is due to kinetic limitations that make it impractical to conduct meaningful sorption measurements at the calculated 1 bar equilibrium temperatures.

Table 1. Comparison of measured and calculated reaction temperatures for the $LiBH_4$/MgX destabilized reaction systems for different X substituents.

X	**Measured Hydrogenation Temperature (°C)[a]**	**Measured Dehydrogenation Temperature (°C)[b]**	**Calculated T(1bar)[c]**
H_2	300	280-400	170
F_2	325	300-450	150
S	350	300-450	175
Se	350	350-450	70

[a] Hydrogenation at 100 bar H_2 during heating at 2°C/min

[b] Dehydrogenation during heating at 2°C/min

[c] Calculated using HSC Chemistry for Windows

An example illustrating hydrogenation and dehydrogenation in a specific $LiBH_4$/MgX system is shown in Figure 13. In this case, H_2 uptake and release vs. temperature are shown together with accompanying composition changes for the $LiBH_4/MgF_2$ destabilized system. Hydrogen sorption measurements were obtained using a custom pressure-volume-temperature system (Sieverts apparatus), and composition changes before and after the sorption cycles were obtained from x-ray diffraction (XRD) measurements. Both hydrogenation and dehydrogenation are clearly evident from the Sieverts data. The accompanying XRD results show the emergence of new phases and changes in composition that occur during the sorption cycles in the destabilized system.

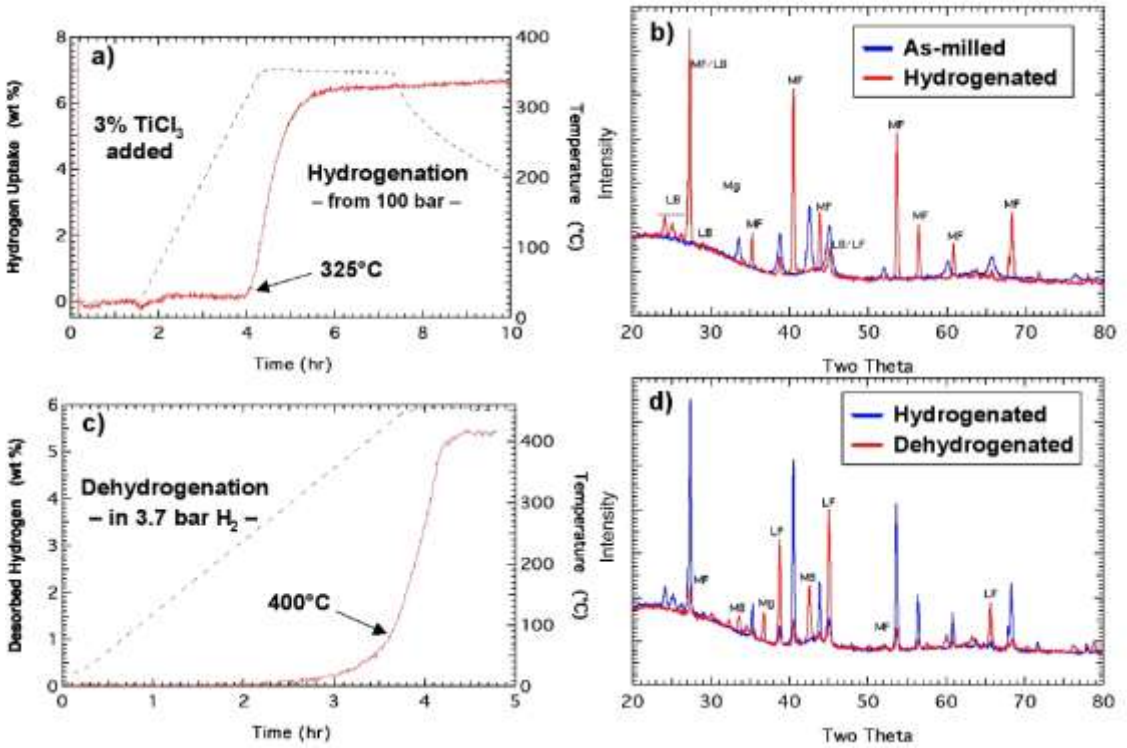

Figure 13: Hydrogenation and dehydrogenation in the $LiBH_4/MgF_2$ destabilized system. a) hydrogen uptake (left ordinate) vs. time during heating (right ordinate) for $LiF+MgB_2$ reaction; b) XRD data before and after hydrogenation. Hydrogenation results in formation of $LiBH_4$ (LB) and MgF_2 (MF) phases; c) Hydrogen desorption (left ordinate) vs. time during heating (right ordinate) from $LiBH_4+MgF_2$; d) XRD data showing formation of LiF (LF) and MgB_2 (MB) upon dehydrogenation.

To try to improve the reversibility of the $LiBH_4/MgF_2$ system we studied the system starting with a mixture of $0.5MgB_2$ + LiF, which represents the dehydrogenated product. The mixture was ball milled for 1 hour and subsequently went through full hydrogenation to form MgF_2 and $LiBH_4$. However, upon dehydrogenation, the reaction was not fully reversible and Mg metal, as opposed to MgB_2, was formed (see Figure 13d). As a result, the capacity for the 2nd cycle hydrogenation was reduced significantly. It was unclear whether thermodynamic or kinetic difficulties were responsible for the capacity fade. To discriminate between these possibilities we increased the mechanical milling time. We showed that full reversibility can be achieved by milling for 10 hr with 3 mol%$TiCl_3$ added as a catalyst. Figure 14 shows hydrogenation profiles of the mixture with and without 3 mol% $TiCl_3$. Without added catalyst, there is a large reduction in the capacity from the 1st to the 2nd cycle. In addition, there is hydrogen uptake a low temperatures (at 1.5 hr) which indicates formation of Mg metal during the dehydrogenation. This is the same behavior observed previously for samples milled for only 1 hr. However, with added catalyst and 10 hr milling there is nearly full retention of the capacity from the 1st to the 2nd cycle and the 2nd and 3rd cycles are identical. In addition, the kinetics improved from the 1st to the 2nd cycle. Overall the capacity on the 1st cycle is lower with added catalyst, which may be due to loss of Li through the formation LiCl from the $TiCl_3/LiBH_4$ reaction. Figure 15 shows the dehydrogenation profiles for the first three

cycles. Addition of the catalyst improved the kinetics of the dehydrogenation reaction as well.

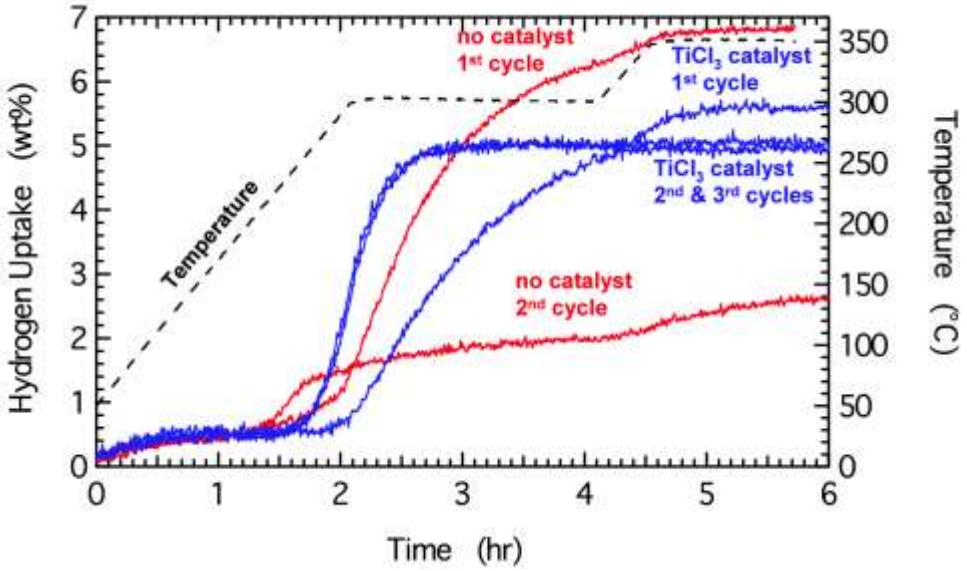

Figure 14: Hydrogenation profiles for the $0.5MgB_2$+LiF system with and without 3% of $TiCl_3$ added as a catalyst. There is a large reduction in capacity in the absence of the catalyst. In addition, the low temperature step on the 2nd cycle indicates the presence of Mg. In the presence of the catalyst, there is small reduction from the 1st to the 2nd cycle but the 2nd and the 3rd cycle show identical hydrogen uptake.

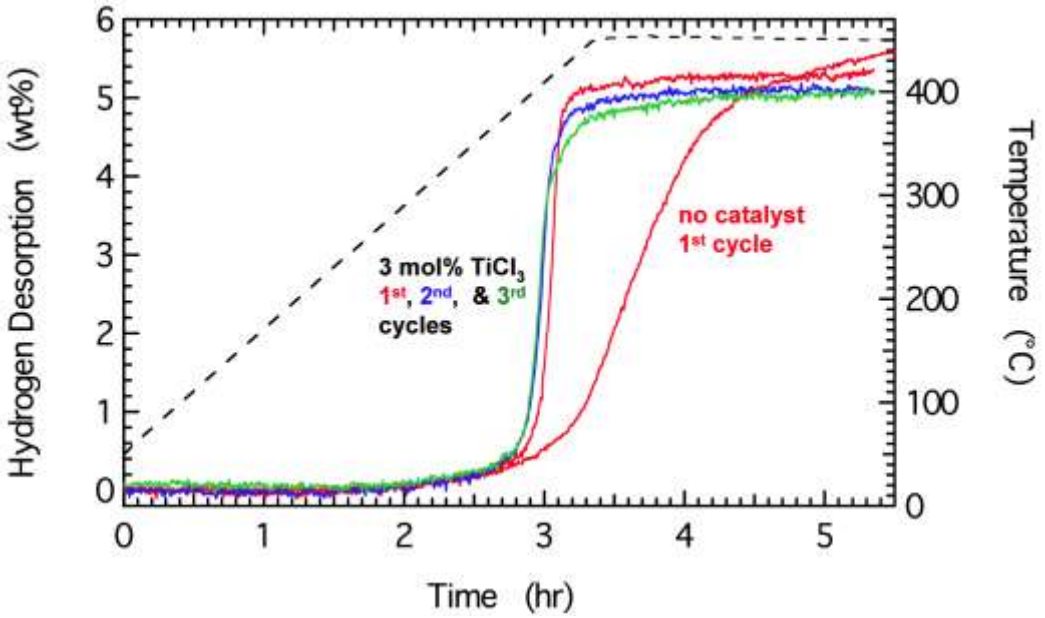

Figure 15: Dehydrogenation profiles for the samples shown in Figure 14. The $TiCl_3$ greatly improves the desorption kinetics as well as cycling stability (the 2nd desorption for the sample without catalyst was not performed since little hydrogen uptake was observed, as shown in Figure 14).

We also examined the following two systems:

- $2LiBH_4 + MgCl_2 \leftrightarrow 2LiCl + MgB_2 + 4H_2$ (5.8 wt.%, $T_{1\ bar} = -10$ °C)

(No H_2 uptake from $2LiCl + MgB_2$ at 150 bar, up to 250°C, possibly because T_{1bar} is too low)

- $4LiBH_4 + Mg_2Cu \leftrightarrow 4LiH + 2MgB_2 + Cu + 6H_2$ (6.0 wt.%)

(From $4LiBH_4 + Mg_2Cu$, only trace MgB_2 is formed , i.e., $4LiBH_4$ and Mg_2Cu did not react with each other)

Unfortunately, neither system showed any reversibility. We believe that the first reaction did not reverse because the reaction kinetics was very slow at low temperatures as dictated by its thermodynamics.

We also investigated the case of X = Si with the assumed reaction being:

- $4LiBH_4 + Mg_2Si \leftrightarrow 4LiH + 2MgB_2 + Si + 6H_2$ (7.3 wt.%, $T_{1bar} = 230$ °C)

A mixture with compositions of $4LiH + 2MgB_2 + Si$ was found to absorb 5.5 wt % H_2 under 100 bar of hydrogen at 350 °C. X-ray diffraction showed the formation of $LiBH_4$ and Mg_2Si upon hydrogenation. However, upon subsequent dehydrogenation Mg_2Si did not react. The most likely explanation is the high chemical stability of Mg_2Si which has been known to be very difficult to hydrogenate.

The final $LiBH_4$/MgX composition examined was with X = I; the expected reaction is:

- $2LiBH_4 + MgI_2 \leftrightarrow 2LiI + MgB_2 + 4H_2$ (2.5 wt.%, $T_{1\ bar} = -20$ °C, $T_{100\ bar} = 120$ °C)

This reaction promises a low weight hydrogen storage capacity. However, studying this reaction might offer new insights into reaction kinetics in destabilized systems. LiI is a known lithium ion conductor. The high mobility of lithium might lead to fast reaction rates. Unfortunately, heating a ball milled mixture of LiI and MgB_2 in 100 bar of hydrogen at 130 ^oC did not lead to any hydrogen uptake. Moreover, no borohydride formation was observed in either XRD or FTIR. The low T_{1bar} of -20 ^oC estimated with the HSC software greatly limits further increase of reaction temperature. However, small errors in thermodynamic data can lead to large variations of T_{1bar}.

5.2.3 Study of destabilized systems containing C, Si, amides, or oxides

We also studied or proposed several systems based on C, Si, amides, or oxides.

The system:

- $4LiBH_4 + C = 4LiH + B_4C + 6H_2$ (12 wt.%, $T_{1\ bar} = 290$ °C)

was tested beginning with LiH and B_4C. No hydrogenation was observed. A similar system we investigated involved the hydrogenation of LiBC. As suggested by the Theory Group (Karl Johnson and David Scholl), the following reaction has a calculated ΔH at 300 K of 31.8 kJ/mol-H_2 and a hydrogen storage capacity of 11.9 %:

- $LiBH_4 + C = LiBC + 2H_2$

We successfully synthesized LiBC from elemental Li, B, and C. Graphite and amorphous boron were milled for one hour followed by addition of small pieces of lithium with hand mixing. The mixture was sintered at 950^oC for four hours in a stainless steel tube sealed with Swagelok caps on both ends. X-ray diffraction patterns of the product matched those of LiBC in the powder diffraction database. Hydrogenation attempts were performed under 100 bar of hydrogen. The system temperature was ramped up at 2^oC/min to 350^oC, held for 3 hours and cooled slowly at 0.25^oC/min to 100^oC. Infrared spectra of the sample after hydrogenation showed no BH_4^- stretches while XRD spectra showed only LiBC.

We further considered $Mg(BC)_2$ as a starting material to investigate the following destabilized reaction, which was also suggested by the Theory Group:

- $Mg(BH_4)_2 + C = Mg(BC)_2 + 4H_2$

We synthesized $Mg(BC)_2$ from MgB_2 and C. Graphite and MgB_2 were milled for an hour and the mixture was sintered at 975 ^oC for 24 hours in a stainless steel tube sealed with Swagelok caps on both ends. X-ray diffraction patterns of the product match those of $Mg(BC)_2$ in the powder diffraction database (Figure 16). However, there is considerable amount of unreacted graphite. In the meantime, the MgB_2 has been converted into $Mg(B_{0.9}C_{0.1})_2$ which may be an intermediate in the formation of $Mg(BC)_2$. We attempted the hydrogenation of this mixture by cooling extremely slowly under 100 bar of hydrogen from 350 °C to 100 °C at 45 °C/day. Infrared spectra of the mixture did not show any stretches from borohydride anions indicating that no hydrogenation occurred.

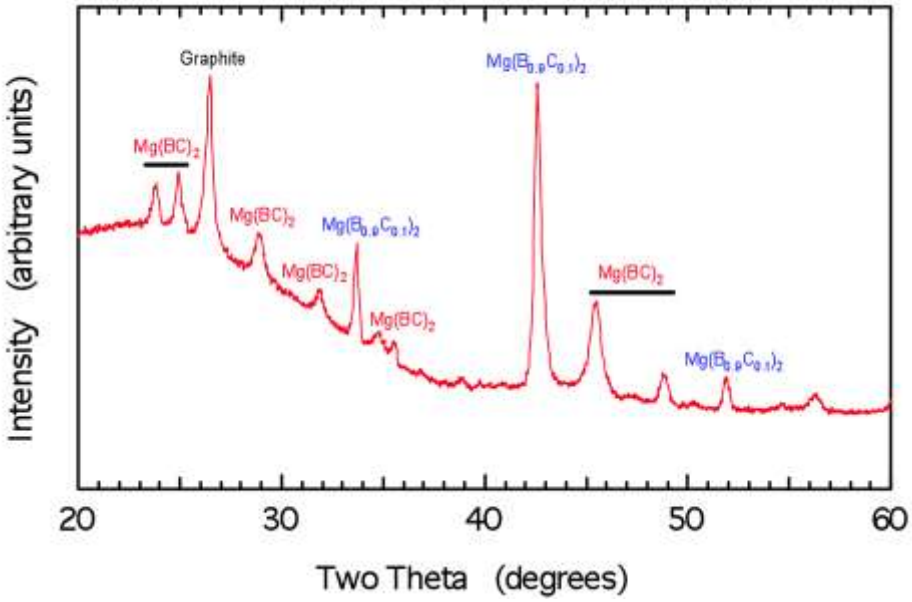

Figure 16: XRD patterns of $Mg(BC)_2$ synthesized from MgB_2 and graphite. There was substantial amount of graphite left. In addition, formation of $Mg(B_{0.9}C_{0.1})_2$ was observed.

Finally, we summarize a few systems that we attempted that did not show reversible hydrogen storage.

The system:

- $LiBH_4 + 1/nSi = LiH + 1/nB_nSi + 1.5H_2$ (n = 1, 2, or 3; 9.5 wt% for n = 3)

was examined beginning with $LiBH_4$ and Si. Upon dehydrogenation, no reaction with the Si, ie no coupling, was observed.

Lithium and Mg amides may be destabilized with Si according to the reactions:

- $2LiNH_2 + Si = Li_2SiN_2 + 2H_2$ (5.4 wt%) and
- $Mg(NH_2)_2 + Si = MgSiN_2 + 2H_2$ (4.7 w%)

Although Li_2SiN_2 was not available, to test this class of reactions we obtained $MgSiN_2$ and $CaSiN_2$ (Rich Kanar, UCLA) and attempted the hydrogenation reactions. No hydrogenation was observed.

Because there are numerous metal oxide compounds and oxygen or water is a likely contaminate during long term cycling we sought reactions based on oxide compounds. Three example reactions are:

- $4LiH + TiO_2 = 2Li_2O + Ti + 2H_2$ (3.6 wt.%, $T_{1\ bar} = 195$ °C)
- $4LiH + SiO_2 = 2Li_2O + Si + 2H_2$ (4.4 wt.%, $T_{1\ bar} = 50$ °C)
- $LiBH4 + SiO_2 = 2LiBO_2 + Si + 2H_2$ (4.9 wt.%, $T_{1\ bar} = 110$ °C)

These reactions were not tested experimentally but were discussed with the theory group for further possible development.

5.2.4 Study of nanoconfined MgH_2

In addition to incorporating $LiBH_4$ within the aerogel, considerable effort was also devoted to incorporating Mg with the ultimate goal of testing the full $LiBH_4/MgH_2$ destabilized system an aerogel. We succeeded in incorporating Mg from molten Mg into aerogels by using a Ni wetting layer. This layer was produced by reduction of a Ni salt, impregnated from an acetone solution. However, the processing temperature of 900 °C led to the formation of graphite as indicated by XRD. The XRD measurements were confirmed by TEM (performed by Channing Ahn, Caltech), which showed considerable breakdown of the aerogel structure, see Figure 17a. By using larger particle size Mg, the impediments to obtaining an acceptable melt imposed by the surface oxide layer on the Mg particles were reduced and good incorporation was achieved at 700 °C. Although a small graphite diffraction feature was still discernable by XRD (data not shown), TEM images of samples with 10 wt% Mg were indistinguishable from unfilled samples (Figure 17b).

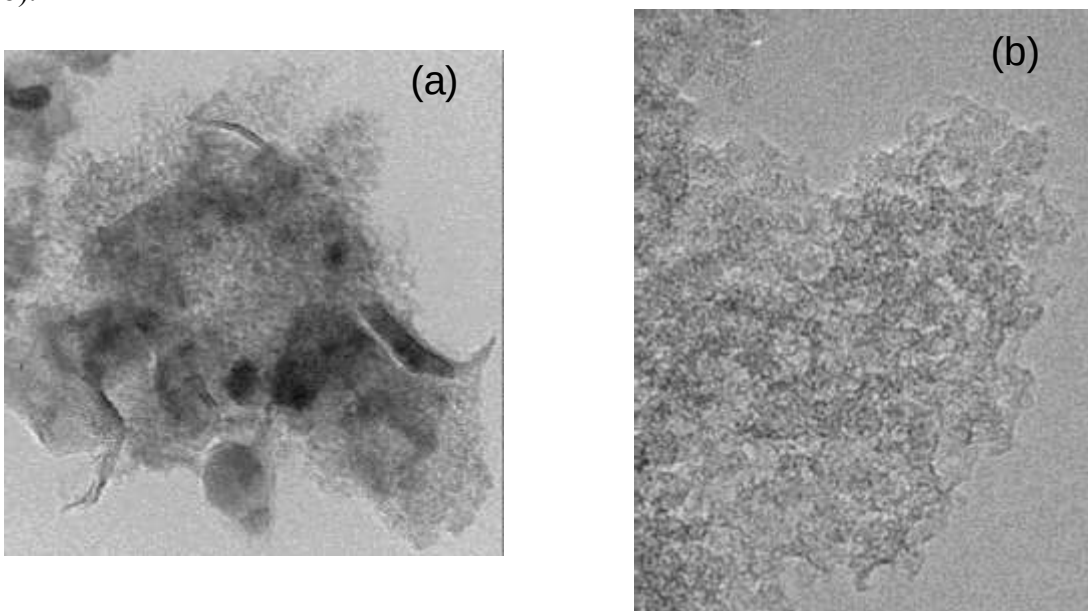

Figure 17: Transmission electron micrographs for 13 nm aerogels containing 10 wt% Mg. For panel (a), the Mg was incorporated into the aerogel from a melt at 900 °C. This temperature caused degradation of the aerogel structure. For panel (b), the Mg was incorporated at 700 °C. The micrograph appears unchanged from an empty aerogel.

The same recipe, heating the aerogel at 700 ^{o}C for 24 hours in the presence of molten Mg, was also extended to aerogels with or without pre-loaded Cu. Similar to Ni, the Cu layer is expected to facilitate the introduction of Mg into the aerogel. However, Cu is not expected to offer significant catalytic activities for hydrogen exchange reactions as Ni does. As will be discussed below, this difference is important in de-convoluting the effects of confinement and catalysis on hydrogen exchange reactions.

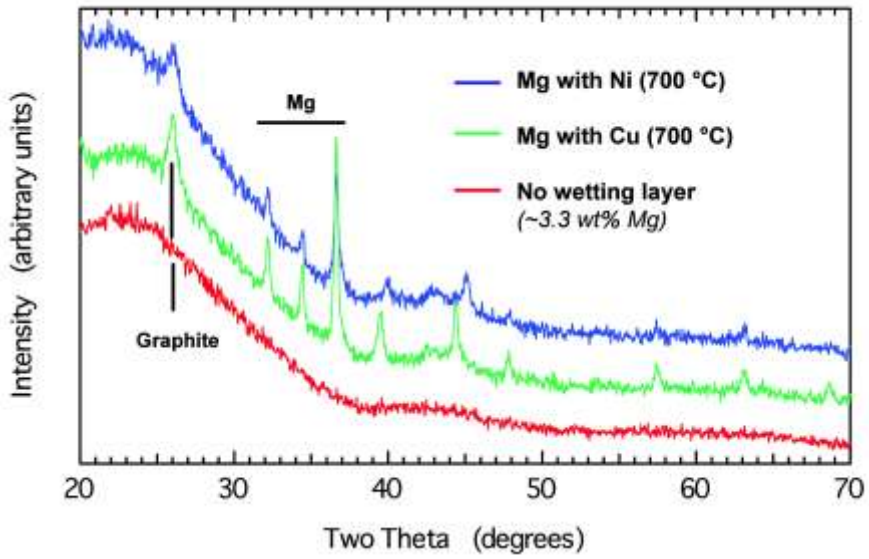

Figure18: XRD patterns of Mg containing carbon aerogel with Ni, Cu, or no metal as the wetting layer. The Mg loadings for Ni and Cu pre-wetted samples are ~ 10% and 3.3% for the sample with no wetting layer.

Figure 18 shows X-ray diffraction patterns for the three materials. Without any wetting layer, only ~3.3 wt% of Mg was introduced after 24 hours at 700 ^{o}C. There are no diffraction peaks in the spectrum. For aerogels pre-wetted with Ni or Cu, about 10 wt% of Mg was introduced. XRD patterns show the presence of Mg as well as broad peaks that can be attributed to graphite. The peak intensities are much lower than the materials prepared previously at 900 ^{o}C, indicating much lower degree of change in carbon aerogel structure. A preliminary analysis of the Mg peak widths, using the Scherrer method, indicated a Mg crystallite size of ~50 nm. Because this crystallite size is much larger than the pore size of the aerogel, we are still uncertain if Mg is being incorporated into the aerogel without damage. One possibility is that the narrow Mg diffraction peaks result from a minority of large Mg crystallites that formed on the exterior surfaces of the aerogel particles.

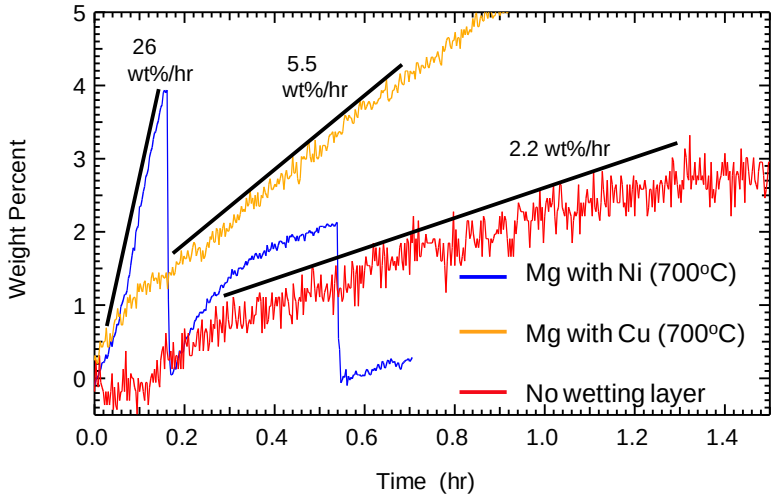

Figure 19: Dehydrogenation at 250 °C of MgH_2 incorporated into aerogels using different wetting layers. For Ni and Cu wetting layers, the aerogel contain 10 wt% Mg and the dehydrogenation rates are 26 wt% Mg/hr and 5.5 wt% Mg/hr, respectively. Without a wetting layer, 3.3 wt% Mg was incorporated and the dehydrogenation rate is 2.2 wt% Mg/hr.

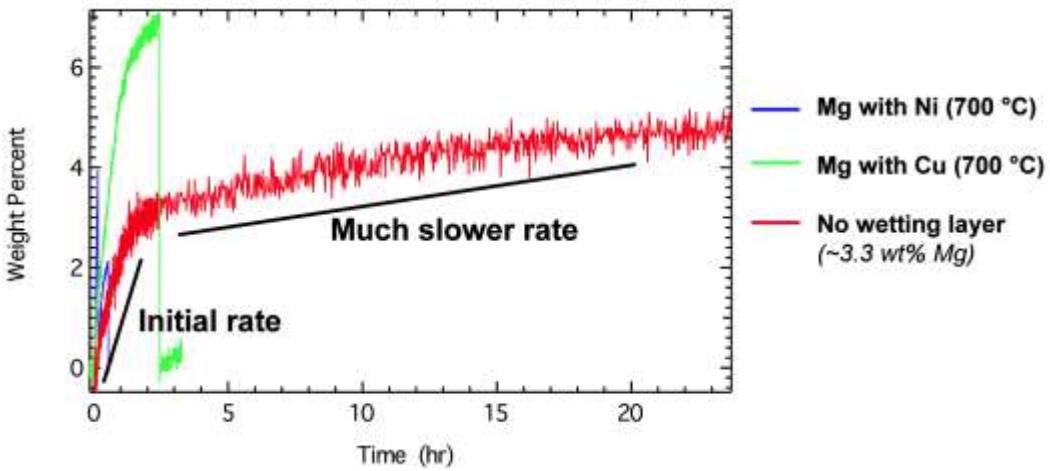

Figure 20: Extended hydrogen desoprtion profiles as shown in Figure 19. The dehydrogenation rate for the sample with no wetting layer decreases dramatically after 3 wt% of hydrogen desorbed. In contrast, the other two materials maintain a constant desorption rate.

We subsequently measured the hydrogen exchange reaction rates of the three samples as shown in Figure 19. At 250 °C, the initial dehydrogenation rates are 25, 5.5, and 2.2 wt%/hour for aerogels preloaded with Ni, Cu, or no metal, respectively. These results clearly demonstrate the catalytic effect of Ni and Cu. An unusual observation with the Mg only sample is a drastic reduction in dehydrogenation rate after the initial fast reaction (Figure 20). In contrast, the dehydrogenation rate does not change for samples with Ni or Cu. The cause for this behavior is under investigation. It is important to point out that the sample containing no Ni or Cu still exhibits a dehydrogenation rate far better than bulk Mg. Consequently, we can conclude that both catalysts and aerogel confinement can greatly accelerate the hydrogen exchange reaction.

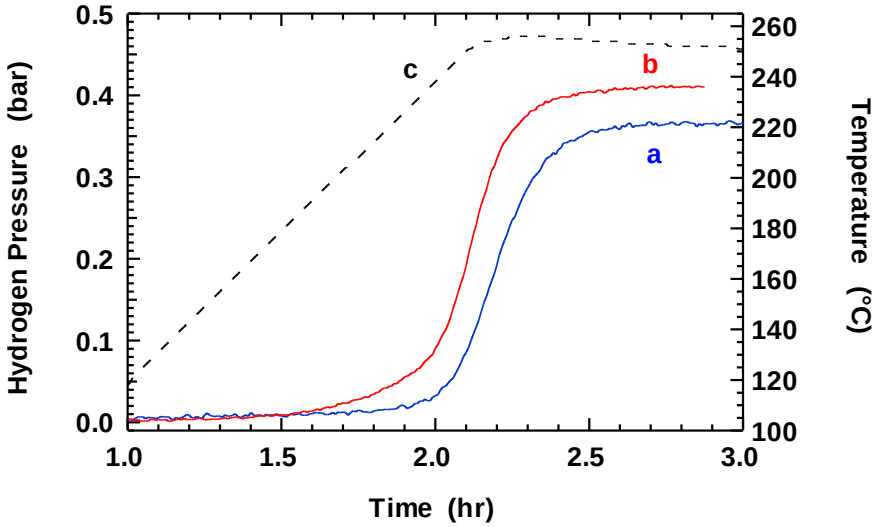

Figure 21: Hydrogen pressure from dehydrogenation of MgH_2 confined in carbon aerogel. (a) MgH_2 confined within 25 nm mode pore size aerogel. (b) MgH_2 within 13 nm aerogel. (c) temperature.

We also performed single-point equilibrium hydrogen pressure measurements at ~250 °C for MgH_2 nano-confined within 13 nm and 25 nm mode pore size carbon aerogels. This data is shown in Figure 21. For these measurements, the sample mass and dehydrogenation volume were adjusted so that a hydrogen pressure of ~0.4 bar would be reached with ~2 wt% hydrogen desorbed, ie, H/Mg ~1.5 assuming a maximum capacity of 7.6 wt%. During the temperature ramp to 250 °C, dehydrogenation begins at 185 °C for the 13 nm sample and 225 °C for the 25 nm sample. The difference indicates enhanced dehydrogenation kinetics for confinement within smaller pores. In addition, the measured pressure at 252 °C is ~10% higher for the 13 nm pore size sample (0.41 versus 0.37 bar). This could indicate a slight destabilization of MgH_2. However, the pressure for the 13 nm sample is nearly identical to the equilibrium pressure for bulk MgH_2 determined from the Sandia hydride database (0.44 bar). Thus, it is uncertain whether there is a significant change in the thermodynamic properties for MgH_2 confined within 13 nm pores.

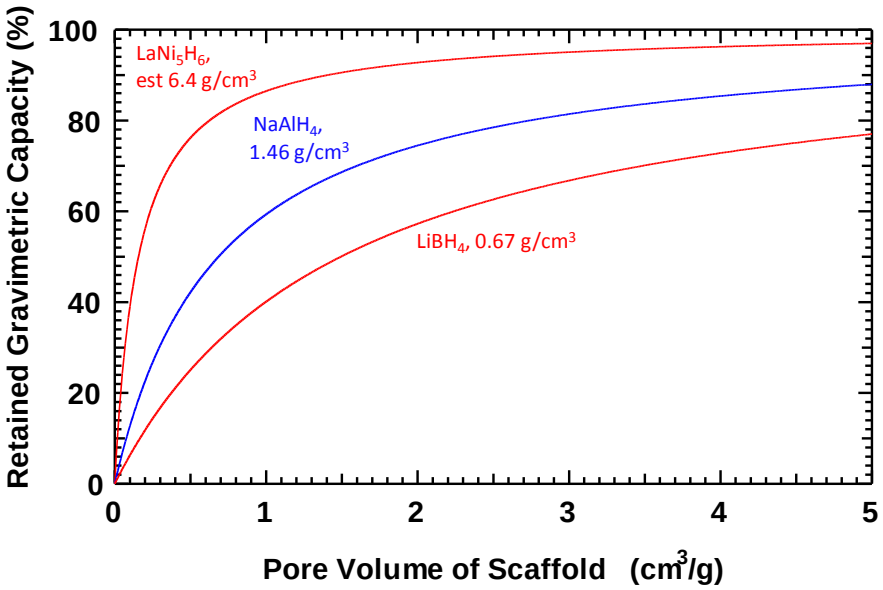

Figure 22: Retained gravimetric capacity for hydrides nano-confined within scaffold hosts. Capacities are shown versus scaffold pore volume for selected hydride densities.

However, recently, precise equilibrium pressure measurements showed an ~12% increase in the equilibrium pressure at 330 °C for the nanosize MgH_2 relative to bulk MgH_2. The enthalpy was determined to decrease by 2.84 kJ/mol-H_2, from 74.06 ± 0.42 kJ/mol-H_2 for the bulk to 71.22 ± 0.49 kJ/mol-H_2 for 7 nm crystals. The entropy also decreased from 133.4 ± 0.7 J/k-mol-H_2 to 129.6 ± 0.8 J/k-mol-H_2. Based on these recent parameters, the equilibrium pressures at 252 °C are calculated to be 0.40 bar for bulk MgH_2 and 0.48 bar for 7 nm nano-MgH_2, an ~20% increase. Using these values, the ~10% increase shown in Figure 21 may indeed represent a slight destabilization for, 13 nm sized MgH_2, relative to 26 nm MgH_2.

5.2.5 Practical consideration of using scaffolds for nanoconfinement

In addition to favorably altering the thermodynamics and/or the kinetics of a confined hydride, use of a scaffold must be practical when considering the overall gravimetric and volumetric hydrogen capacities and the chemical and mechanical stabilities during cycling. The scaffold pore size, topology, and surface chemistry must be optimized for the hydride thermodynamics and kinetics; the specific pore volume must be optimized for the overall capacities; and the scaffold composition must be optimized for stability.

Ideally, the scaffold itself would also store hydrogen and contribute to the storage capacity. However, this is extremely challenging, and thus far, the scaffolds studied simply contribute extra weight to the system, thereby reducing both the gravimetric and volumetric capacities. To be practical, the reduction in capacities must be minimized. The gravimetric capacity including the mass of the scaffold relative to the bulk capacity [$C_{G,scaffold}$ /$C_{G,bulk}$] depends on the hydride density [$\rho_{hydride}$ (g/cm^3)] and the specific pore volume of the scaffold [PV (cm^3/g)]. This dependence, expressed as a percentage and denoted as the Retained Gravimetric Capacity, is given by

$C_{G,scaffold}/ C_{G,bulk} = 100\% \bullet \rho_{hydride} \bullet PV / (\rho_{hydride} \bullet PV + 1)$

A plot of the Retained Gravimetric Capacity as a function of scaffold pore volume for different hydride materials is shown in Figure 22. Overall, the retained capacity is increased for larger pore volume scaffolds and denser hydride materials. For example, if a scaffold were used to confine $LaNi_5H_6$, which has a relatively high density of 6.4 g/cm^3, the retained capacity could be >80% for a scaffold with a pore volume of ~1 cm^3/g. In contrast, for $LiBH_4$, which has one of the lowest densities of any hydride, a pore volume of ~4 cm^3/g is required for a retained capacity of 70%. The scaffolds used in the studies described above have specific pore volumes of 0.5 – 1.5 cm^3/g (See Figure 3). However, much larger specific pore volumes are possible. For example, aerogels can be synthesized with pore volumes >4 cm^3/g. The challenge will be combining a sufficient pore volume with the desired pore size in a structurally stable scaffold capable of withstanding multiple sorption cycles.

Similarly, the Retained Volumetric Capacity [$C_{V,scaffold} /C_{V,bulk}$] depends on the scaffold density [$\rho_{scaffold}$ (g/cm^3)] and the pore volume as given by

$C_{V,scaffold} /C_{V,bulk} = 100\% \bullet \rho_{scaffold} \bullet PV / (\rho_{scaffold} \bullet PV + 1)$

A plot of the Retained Volumetric Capacity for carbon-based scaffolds is given in Figure 23. From this plot, ~80% retained capacity can be achieved using carbon scaffolds with pore volumes of 1.5 – 2 cm^3/g. Thus, for low-density hydride materials, retaining the volumetric capacity places a lower requirement on the scaffold pore volume than the gravimetric capacity. Overall, it appears that nano-confined hydride materials with ~80% retained capacities are feasible.

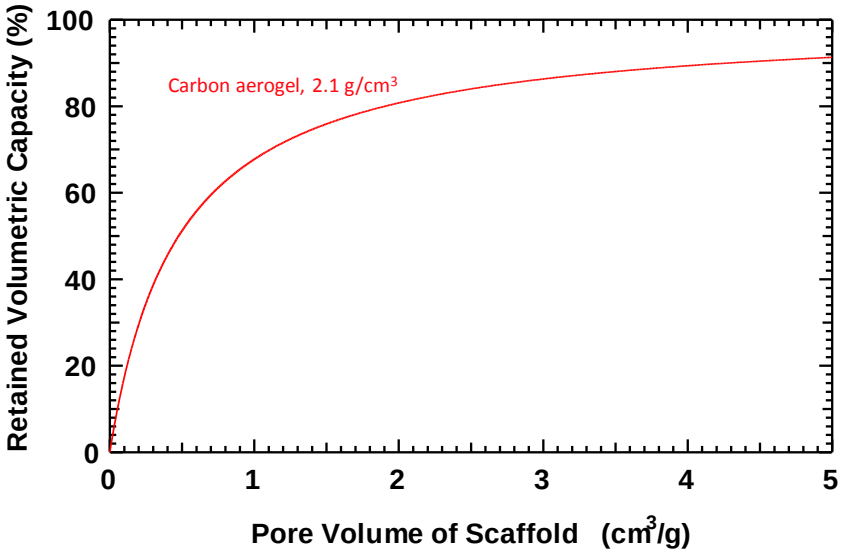

Figure 23: Retained volumetric capacity for hydrides nano-confined within scaffold hosts. Capacities are shown versus scaffold pore volume for a scaffold density of 2.1 g/cm^3, which is typical for porous carbon materials including carbon aerogel.

Because studies of nano-confinement using porous hosts is still in the beginning stages, little work has addressed chemical or mechanical stability during long term cycling. Ideally, for chemical stability, the scaffold would be thermodynamically stable with respect to hydrogen and the confined hydride. This goal favors strongly bound oxides, such as MgO or ZrO_2. However, these materials are not currently available as appropriate porous scaffold hosts. Alternatively, carbon-based scaffolds, which are available in a wide variety of nanoporous forms, have been most frequently used. These materials combine moderate thermodynamic stability with high kinetic stability. As mentioned above for MgH_2 confined within carbon aerogel, ten hydrogen exchange cycles were performed without noticeable degradation. For $LiBH_4$ confined in carbon aerogel, preliminary measurements of CH_4 formation during dehydrogenation were conducted using FTIR as shown in Figure 24. Methane formation was clearly detected, although the amount was small (<~0.2 wt%). Further work is needed to understand the chemical stability of the scaffolds during repeated cycling.

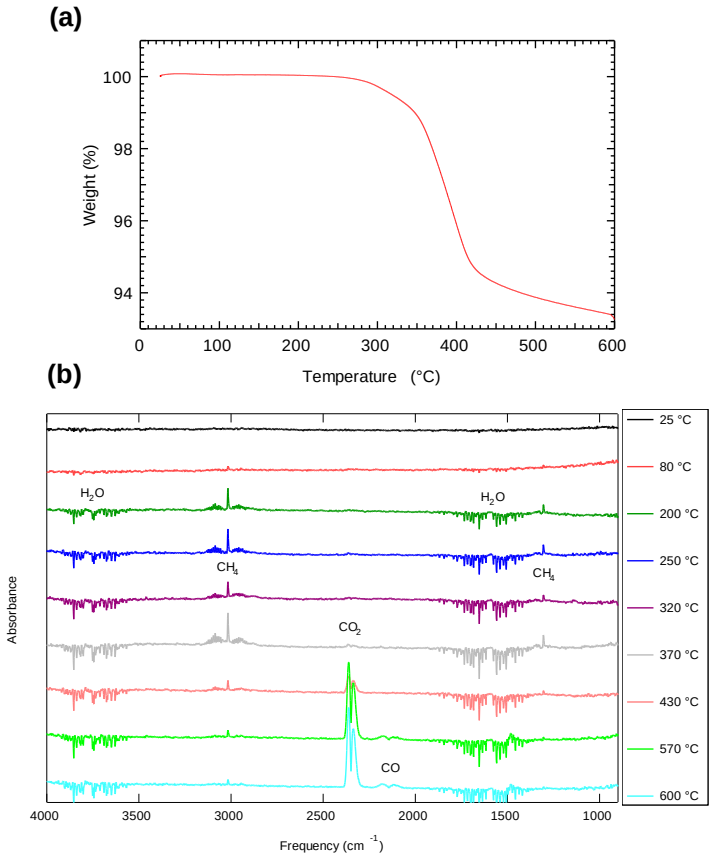

Figure 24: TGA (panel a) and FTIR (panel b) for dehydrogenation of $LiBH_4$ incorporated into 25 nm aerogel. FTIR spectra were measured from the evolved gas at the temperatures shown. The (negative) peaks for water likely result from water being purged from the gas flow lines and are not associated with the sample. The CO and CO_2 may result from oxidation of the aerogel from residual organic species. Evolution of methane is clearly seen. The amount of methane represented by the FTIR spectra, has not been completely quantified. However, there is methane at 200 °C but almost no mass loss. This indicates that the FTIR analysis is very sensitive to methane. From the actual rate of mass loss at 200 °C, which is ~0.00054 wt%/°C, we estimate that the total amount of methane over the whole temperature range is <~ 0.2 wt%. This value is an upper limit because we assumed that all of the mass loss at 200 °C (0.00054 wt%/°C) was due to methane.

6. Products

Publications

1. J. J. Vajo and G. L. Olson, "Hydrogen Storage in Destabilized Chemical Systems" (Invited "Viewpoint Set" article) *Scripta Materialia*, **56** 829-834 (2007).
2. J.J. Vajo, T.T. Salguero, A.F. Gross, S.L. Skeith, and G. L. Olson "Destabilization Strategies and Kinetics Challenges in Light Metal Hydride Systems" *J. Alloys and Compounds*, **446 – 447** 409 – 414 (2007).
3. A.F. Gross, J.J. Vajo, S.L. Skeith, and G.L Olson, "Enhanced hydrogen storage kinetics of $LiBH_4$ in nanoporous carbon scaffolds", *J. Phys. Chem. C.,* **112**, 5651 – 5657 (2008).
4. A.F. Gross, C. C. Ahn, S. L. Van Atta, P. Liu, J. J. Vajo, "Fabrication and hydrogen sorption behavior of nanoparticulate MgH_2 confined in a porous carbon host", *Nanotechnology,* **20**, 204005 (special issue focused on nanoscale phenomenon in hydrogen storage).
5. J. Graetz, S. Chaudhuri, T. T. Salguero, J. J. Vajo, M. S. Meyer, F. E. Pinkerton, "Local bonding and atomic enviroments in Ni-catalyzed complex hydrides" *Nanotechnology*, **20**, 204007 (special issue focused on nanoscale phenomenon in hydrogen storage).
6. J. Purewal, H. Kabbour, J. J. Vajo, C. C. Ahn, B. Fultz, "Pore size distribution and supercritical hydrogen adsorption in activated carbon fibers", *Nanotechnology,* **20**, 204012 (special issue focused on nanoscale phenomenon in hydrogen storage).
7. S. T. Kelly, B. M. Clemens, S. L. Van Atta, J. J. Vajo, G. L. Olson, "Kinetic limitations of the Mg_2Si system for reversible hydrogen storage" *Nanotechnology,* **20***,* 204017 (special issue focused on nanoscale phenomenon in hydrogen storage).
8. S. Zhang, A. F. Gross, S. L. Van Atta, M. Lopez, P. Liu, C. C. Ahn, J. J. Vajo, C. M. Jensen, Synthesis and hydrogen storage properties of MgH_2 incorporated carbon aerogel scaffold", *Nanotechnology,* **20***,* 204027 (special issue focused on nanoscale phenomenon in hydrogen storage).
9. H. Wu, W. Zhou, K. Wang, T. J. Udovic, J. J. Rush, T. Yildirum, L. A. Bendersky, A. F. Gross, S. L. Van Atta, J. J. Vajo, F. E. Pinkerton, "Size effects on hydrogen storage properties of nanoscaffolded $Li_3BN_2H_8$" , *Nanotechnology ,* **20***,* 204002 (special issue focused on nanoscale phenomenon in hydrogen storage).
10. R. D. Stephens, A. F. Gross, S. L. Van Atta, J. J. Vajo and F. E. Pinkerton, "The kinetic enhancement of hydrogen cycling in NaAlH4 by melt infusion into nanoporous carbon aerogel", *Nanotechnology ,* **20***,* 204018 (special issue focused on nanoscale phenomenon in hydrogen storage).
11. W. Li, J. J. Vajo, R. W. Cumberland, P. Liu, S.-J. Hwang, C. Kim, R. C. Bowman, Jr., "Hydrogenation of magnesium nickel boride for reversible hydrogen storage", *J. Phys. Chem. Lett.* **1**, 69 – 72 (2010).

12. J.J. Vajo, Wen Li, and P. Liu, "Thermodynamic and Kinetic Destabilization in $LiBH_4/Mg_2NiH_4$: Promise for Borohydride-Based Hydrogen Storage", Chem. Comm., 46, 6687-6689 (2010)
13. J.J. Vajo, "Influence of nano-confinment on the thrermodynamics and dehydrogenation kinetics of metal hydrides" Current Opinion in Solid-State and Materials Science, Submitted (2010).

Presentations

1. J.J. Vajo, "Destabilization of Strongly Bound Hydrides for Hydrogen Storage Applications" (invited presentation) Gordon Research Conference Hydrogen-Metal Systems Waterville, ME, (July 10-15, 2005).
2. G.L. Olson, J.J. Vajo, A.F. Gross, T. M. Salguero, S.L. Skeith, and B. M. Clemens, *"Nanostructure Engineering for Improved Reaction Rates in Destabilized Hydrides"* (poster presentation) Gordon Research Conference Hydrogen-Metal Systems Waterville, ME, (July 10-15, 2005).
3. G.L. Olson and J.J. Vajo "*Destabilized Hydrides"* presentation to FreedomCAR Hydrogen Storage Tech Team (1/12/2006).
4. F. Gross, J.J. Vajo, S.L. Skeith, and G.L Olson, "*Enhanced Hydrogen Storage Properties of Metal Hydrides using Nanoporous Carbon Scaffolds"* at American Chemical Society Meeting, Atlanta, GA (March 27-31, 2006).
5. J.J. Vajo, T.T. Salguero, A.F. Gross, S.L. Skeith, and G. L. Olson, "Kinetics and Thermodynamics of Destabilized Hydride Systems" (invited presentation) Materials Research Society Spring Meeting, San Francisco, CA (April 17-21, 2006).
6. J.J. Vajo, T.T. Salguero, A.F. Gross, S.L. Skeith, and G. L. Olson "Destabilization Strategies and Kinetics Challenges in Light Metal Hydride Systems" (Invited presentation at MH2006 Conference, Lahaina, Hawaii, Oct. 1-6, 2006).
7. A. F. Gross, "*Synthesis and Characterization of Nanoscale $LiBH_4$ for Hydrogen Storage Applications*" Invited presentation, California State University Northridge, March 2007.
8. J.J. Vajo, A.F. Gross, R.D. Stephens, T.T. Salguero, S.L. Van Atta, and P. Liu, "Hydride Chemistry in Nanoporous Scaffolds", Invited presentation, International Symposium on Materials Issues in a Hydrogen Economy, November 12-15, 2007, Richmond, Virginia.
9. A.F. Gross, S.L. Skeith, P. Liu, and J.J. Vajo, "Fabrication and Characterization of Nanoscale MgH_2 for Hydrogen Storage Applications" MRS Fall Meeting, November 2007, Boston, MA.
10. J.J. Vajo, A.F. Gross, R.D. Stephens, T.T. Salguero, S.L. Van Atta, and Ping Liu, "Nanoscale Hydrides in Porous Carbon Scaffolds", Invited presentation, APS Spring Meeting, March 2008, New Orleans, LA.
11. J. J. Vajo, "Hydrogen Storage for Transportation Applications", Invited presentation, ASM International San Fernando Valley Chapter: Alternative Energy Mini Symposium, April 2008, Northridge, CA.
12. J. J. Vajo, "Hydrogen storage for transportation applications", Invited presentation, ASM International San Ferando Valley Chapter: Alternative Energy Mini Symposium, April 2008, Northridge, CA.

13. J. J. Vajo, W. Li, P. Liu, “Thermodynamic and kinetic destabilization in $LiBH_4$-based hydride systems”, American Physical Society Meeting, March, 2009, Pittsburg, PA.
14. W. Li, J. J. Vajo, R. W. Cumberland, P. Liu, S.-J. Hwang, C. Kim, “Reversible low temperature hydrogen storage using ternary borides”, American Physical Society Meeting, March, 2009, Pittsburg, PA.
15. J. J. Vajo, A. F. Gross, S. Zhang, S. L. Skeith, P. Liu, C. M. Jensen, Hydrogen storage behavior of $LiBH_4/MgH_2$ confined in nanoporous scaffolds, MRS Fall Meeting, December 2010.

Patents

1. W. Li, J. J. Vajo, P. Liu, “Magnesium based metal borides for reversible hydrogen storage at low temperature” Patent application filed March 2009.
2. A. F. Gross, J.J. Vajo, R.W. Cumberland, P. Liu, and T.T. Salguero, “Metal filled porous carbon”, Patent application filed July 2008.